Plasma Chem Plasma Process (2007) 27:141–162
DOI 10.1007/s11090-006-9047-x

ORIGINAL PAPER

Modeling Study on the Entrainment of Ambient Air into Subsonic Laminar and Turbulent Argon Plasma Jets

Hai-Xing Wang · Xi Chen · Wenxia Pan

Received: 1 December 2006 / Accepted: 2 December 2006 / Published online: 23 February 2007

Abstract Modeling study is performed to reveal the special features of the entrainment of ambient air into subsonic laminar and turbulent argon plasma jets. Two different types of jet flows are considered, i.e., the argon plasma jet is impinging normally upon a flat substrate located in atmospheric air surroundings or is freely issuing into the ambient air. It is found that the existence of the substrate not only changes the plasma temperature, velocity and species concentration distributions in the near-substrate region, but also significantly enhances the mass flow rate of the ambient air entrained into the jet due to the additional contribution to the gas entrainment of the wall jet formed along the substrate surface. The fraction of the additional entrainment of the wall jet in the total entrained-air flow rate is especially high for the laminar impinging plasma jet and for the case with shorter substrate standoff distances. Similarly to the case of cold-gas free jets, the maximum mass flow-rate of ambient gas entrained into the turbulent impinging or free plasma jet is approximately directly proportional to the mass flow rate at the jet inlet. The maximum mass flow-rate of ambient gas entrained into the laminar impinging plasma jet slightly increases with increasing jet-inlet velocity but decreases with increasing jet-inlet temperature.

Keywords Thermal plasma · Impinging and free jets · Jet entrainment · Modeling

H.-X. Wang
School of Astronautics, Beijing University of Aeronautics and Astronautics, Beijing 100083, China

X. Chen (✉)
Department of Engineering Mechanics, Tsinghua University, Beijing 100084, China
e-mail: cx-dem@mail.tsinghua.edu.cn

W. X. Pan
Institute of Mechanics, Chinese Academy of Sciences, Beijing 100080, China

Introduction

Numerous studies have been performed in recent decades concerning the characteristics of thermal plasma jets with jet-inlet temperatures of 10^4 K due to their widespread applications in industries and in labs, such as in plasma spraying, thermal plasma chemical vapor deposition, thermal plasma synthesis, thermal plasma waste destruction, plasma cutting, surface remelting and cladding, etc. Although a large amount of experimental and modeling results have been reported in the literature (see [1–16] and the references cited therein), our understanding about the thermal plasma jet characteristics, especially about the entrainment of ambient gas into the thermal plasma jet, is still incomplete. When a thermal plasma jet is ejected from a plasma torch and issuing freely into an ambient gas originally at rest (so-called submerged plasma jet), the ambient gas will be entrained (or drawn) into the plasma jet due to the momentum transfer between the jet fluid and the ambient gas, leading to the continuous spreading of jet boundary in radial direction, the increase of the total axial mass flux of the plasma jet and the spatial evolution of plasma temperature, axial velocity and species concentration (if the plasma-forming gas is different from the ambient gas) profiles at the jet cross-sections in the direction of jet axis. When the plasma jet is impinging normally upon a solid substrate (or workpiece), as often encountered in thermal plasma materials processing, generally there exist three different regions of distinct flow characteristics in the jet, as shown schematically in Fig. 1, i.e., (i) the free-jet region, in which the ambient gas is entrained but the plasma flow is less influenced by the presence of substrate and the dominant velocity component is axial; (ii) the wall-jet region formed along the substrate surface, in which the dominant velocity component is radial outwards and the boundary layer formed along the substrate surface will thicken in the radial direction; and (iii) the impinging region, which links up the other two regions and is characterized by significant changes of plasma flow direction. The ambient gas is also entrained into the wall-jet region, and such an additional entrainment will increase the gas flow rate entrained into the plasma jet and affect the transport process in the impinging plasma jet. Most experimental and modeling results concerning thermal plasma jet characteristics available in the literature are usually presented in the form of measured or predicted spatial distributions of plasma temperature, velocity (or stream function) and/or species concentration in the plasma jet [1–16], since those distributions of plasma parameters are of significant importance for the control and optimization of the relevant technological processes in thermal plasma materials processing. Although the information about the spatial evolution of plasma

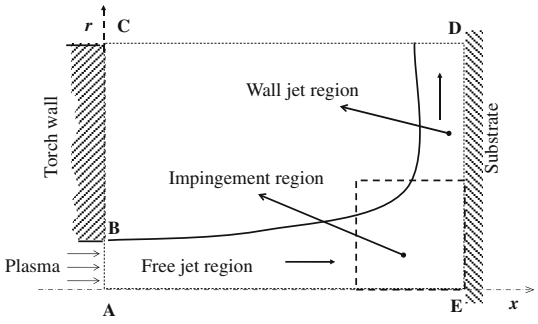

Fig. 1 Schematic of impinging plasma jet and the computational domain used for the impinging plasma jet modeling. DE is the surface of a solid substrate for the impinging jet case, while it is a flow boundary for the free jet case

parameters in the plasma jet reflects the effects of the entrainment of ambient gas on the plasma jet characteristics to a certain extent, from such information it is hard to clarify the law which governs the entrainment rate of ambient gas into the free or impinging plasma jet. The knowledge about the entrainment rate of ambient gas into the free or impinging plasma jet, however, is essential for many cases. For example, the entrainment rate of ambient air into an impinging or free plasma jet will affect the oxidizing of metallic particles injected into the plasma jet or affect the oxidation or nitridation of metallic workpieces in thermal plasma materials processing.

Concerning the entrainment of ambient gas into a laminar or turbulent free gas jet at room temperature, there have been many studies and the laws governing the entrainment of ambient gas into the submerged laminar or turbulent free jets have been well established. Those studies are helpful for us to understand the entrainment of ambient gas into the thermal plasma jet and thus here we review them briefly. For an axisymmetrical *laminar* jet issuing from a nozzle and flowing freely into a quiet ambient fluid with the same fluid type and temperature, Refs. [17, 18] showed analytically that the axial variation of the total mass flow rate of the jet due to the entrainment of ambient fluid into the laminar free jet could be expressed as

$$\frac{\mathrm{d}F}{\mathrm{d}x} = 8\pi\mu \tag{1}$$

where F is the local axial mass flux (or mass flow rate) of the laminar free jet at the axial distance x measured from the jet inlet, $\mathrm{d}F/\mathrm{d}x$ is the entrainment rate per unit of jet length, and μ is the fluid viscosity. On the other hand, for an axisymmetrical *turbulent* gas jet issuing freely into a similar or dissimilar ambient gas with the same temperature, experimental studies were carried out in Refs. [19, 20] using a specially designed porous chamber technique and showed that the local entrainment rate per unit of jet length at the axial location x could be expressed as

$$\frac{\mathrm{d}F}{\mathrm{d}x} = C\frac{F_0}{D_0}\left(\frac{\rho_\mathrm{a}}{\rho_0}\right)^{1/2} \tag{2}$$

in which F_0, D_0 and ρ_0 are the mass flow rate, jet diameter and gas density at the jet inlet, whereas ρ_a is the density of ambient gas. Dimensionless factor C is the so-called entrainment coefficient, which was shown being increasing from about 0.1 at the location near the turbulent jet inlet to a constant value 0.32 for the fully developed turbulent region with an initial developing-region dimensionless-length x / D_0 in the range from ~13 to ~35, depending on the velocity profile at the jet inlet (smaller x/D_0 value of the developing turbulent region corresponds to a top-type velocity profile) [21].

Obviously the law governing the entrainment of ambient gas into the laminar free jet shown in Eq. (1) is quite different from that into the turbulent free jet shown in Eq. (2). As is seen from Eq. (1), for the *laminar* free jet at room temperature, the entrainment rate per unit of jet length ($\mathrm{d}F/\mathrm{d}x$) is directly proportional to the fluid viscosity, but independent of the axial distance x and of the mass flow rate and jet diameter at the jet inlet. On the other hand, $\mathrm{d}F/\mathrm{d}x$ for the *turbulent* free jet is directly proportional to the mass flow rate at the jet inlet and inversely proportional to the jet inlet diameter, as seen from Eq. (2). The difference between the laminar and turbulent jets in their entrainment laws is due to that different entrainment mechanisms

are involved in the two types of jets, i.e., molecular transport mechanism is associated with the laminar jet while turbulent transport mechanism is dominant in the turbulent jet.

The direct measurement of the entrainment rate is rather difficult for the impinging jet, although some experimental results were presented in the form of measured or visualized flow fields for impinging jets at room temperature (e.g., see [22, 23]). An analytical solution was given in [24] concerning the laminar radial wall-jet at room temperature, but it is only applicable to the wall-jet region far away from the impinging region. It was showed that the flow rate of ambient gas entrained into the radial wall jet is directly proportional to $(rP\ \mu^3)^{1/4}$, where r is the radial distance from the central stagnation point of the impinging jet, μ is the gas viscosity, whereas P is a parameter proportional to the characteristic velocity and to the square of volumetric flow rate of the jet [24]. Analytical [24] and experimental [25] studies were also performed concerning the turbulent radial wall-jet at room temperature, although no explicit expression of the entrained gas flow rate was given. Modeling results are also available for the flow fields in laminar or turbulent impinging jets [26–28], but from those results one cannot clarify the laws governing the entrainment rate of ambient fluid into the laminar and turbulent impinging jets.

The thermal plasma jets encountered in practical applications are mostly in the turbulent flow state. However, long laminar plasma jets have been generated successfully in recent years using elaborately designed DC non-transferred arc plasma torches [29–31]. From the viewpoint of plasma materials processing, the long laminar plasma jet has a few attractive merits, including its stable flow state, low noise emission, small axial gradients of plasma temperature and axial-velocity, adjustable jet flow-field characteristics, etc. Preliminary attempts to use the laminar plasma jet in materials processing, including the re-melting or cladding hardening of metallic surfaces and the preparation of thermal barrier coating, have shown encouraging results [32–34]. With the thermal plasma materials processing as the main research background, Ref. [35] carried out a systematic modeling study to compare the characteristics of the subsonic turbulent and laminar argon plasma jets issuing freely into atmospheric-pressure air surroundings. It was found that since only the molecular diffusion is involved in the laminar plasma jet, the mass flow rate of the ambient air entrained into the laminar plasma jet is comparatively small and less dependent on the jet inlet velocity. On the other hand, since turbulent transport is dominant in the turbulent plasma jet, the mass flow rate of entrained ambient air is about one order of magnitude larger than its laminar counterpart and approximately directly proportional to the mass flow rate at the jet inlet. As a result, the characteristics of laminar free plasma jets are quite different from those of turbulent free plasma jets. For instance, it is predicted that the length of the high-temperature region of the laminar free plasma jet is considerably long and increases notably with increasing jet-inlet velocity or jet-inlet temperature, while the length of the high-temperature region of the turbulent free plasma jet is much shorter and less influenced by the jet inlet velocity or inlet temperature, in consistence with available experimental observation [31, 36].

As a continuation of Ref. [35], this paper mainly studies the characteristics of the subsonic turbulent and laminar argon plasma jets impinging normally upon a solid substrate located in atmospheric-pressure air surroundings. Especially the entrainment rates of ambient air into the impinging plasma jets (turbulent or laminar) will be examined in some detail and compared with their counterparts into the free plasma jets. It is expected that the presence of the substrate not only affects

appreciably the plasma temperature, velocity and species concentration distributions in the near-substrate region of the plasma jets, but also affects the air entrainment into the argon plasma jets due to the additional contribution to the gas entrainment of the wall jet formed along the substrate surface. The modeling approach used in this study will be described at first. Typical modeling results and discussion are then presented and followed by conclusions.

Modeling Approach

Almost the same modeling approach as used in [35] is employed in the present study. The main change is concerned with the downstream boundary conditions of the plasma jet, i.e., solid wall conditions are used at the downstream boundary for the impinging plasma jet instead of the one-way conditions for the free plasma jet used in [35], in order to reveal the effects of the presence of the substrate on the characteristics of impinging plasma jets, especially on the entrainment rate of ambient air into the impinging argon plasma jets.

The main assumptions employed in this study include (i) the flow is subsonic, steady and axisymmetrical; (ii) the plasma is in the local thermodynamic equilibrium (LTE) state and optically thin to radiation; (iii) the swirling velocity component is negligible in comparison with the axial velocity; (iv) the effect of natural convection on the plasma jet characteristics can be neglected [37, 38]; and (v) the diffusion of the surrounding air into the argon plasma jet can be handled using the combined-diffusion-coefficient method [39, 40] for the laminar case and using the turbulence-enhanced combined-diffusion-coefficient method [13] for the turbulent case.

Based on the foregoing assumptions, the mass, momentum, energy and species conservation equations for the *laminar* case can be written as follows [35, 41, 42]:

$$\frac{\partial}{\partial x}(\rho u)+\frac{1}{r}\frac{\partial}{\partial r}(r\rho v)=0 \tag{3}$$

$$\frac{\partial(\rho uu)}{\partial x}+\frac{1}{r}\frac{\partial(r\rho uv)}{\partial r}=-\frac{\partial p}{\partial x}+2\frac{\partial}{\partial x}\left(\mu\frac{\partial u}{\partial x}\right)+\frac{1}{r}\frac{\partial}{\partial r}\left[r\mu\left(\frac{\partial u}{\partial r}+\frac{\partial v}{\partial x}\right)\right] \tag{4}$$

$$\frac{\partial(\rho uv)}{\partial x}+\frac{1}{r}\frac{\partial(r\rho vv)}{\partial r}=-\frac{\partial p}{\partial r}+\frac{\partial}{\partial x}\left[\mu\left(\frac{\partial v}{\partial x}+\frac{\partial u}{\partial r}\right)\right]+\frac{2}{r}\frac{\partial}{\partial r}\left(r\mu\frac{\partial v}{\partial r}\right)-2\mu\frac{v}{r^2} \tag{5}$$

$$\begin{aligned}\frac{\partial(\rho uh)}{\partial x}+\frac{1}{r}\frac{\partial(r\rho vh)}{\partial r}&=\frac{\partial}{\partial x}\left[\frac{k}{c_p}\frac{\partial h}{\partial x}\right]+\frac{1}{r}\frac{\partial}{\partial r}\left[r\frac{k}{c_p}\frac{\partial h}{\partial r}\right]-U_r-\frac{\partial}{\partial x}[(h_A-h_B)J_x]\\&-\frac{1}{r}\frac{\partial}{\partial r}[r(h_A-h_B)J_r]-\frac{\partial}{\partial x}\left[\frac{k}{c_p}(h_A-h_B)\frac{\partial f_A}{\partial x}\right]-\frac{1}{r}\frac{\partial}{\partial r}\left[r\frac{k}{c_p}(h_A-h_B)\frac{\partial f_A}{\partial r}\right]\\&+u\frac{\partial p}{\partial x}+v\frac{\partial p}{\partial r}+\mu\left\{2\left[\left(\frac{\partial u}{\partial x}\right)^2+\left(\frac{\partial v}{\partial r}\right)^2+\left(\frac{v}{r}\right)^2\right]+\left(\frac{\partial u}{\partial r}+\frac{\partial v}{\partial x}\right)^2\right\}\end{aligned} \tag{6}$$

$$\frac{\partial(\rho u f_A)}{\partial x}+\frac{1}{r}\frac{\partial(r\rho v f_A)}{\partial r}=\frac{\partial}{\partial x}\left[\Gamma_f\frac{\partial f_A}{\partial x}\right]+\frac{1}{r}\frac{\partial}{\partial r}\left[r\Gamma_f\frac{\partial f_A}{\partial r}\right]+S_f \tag{7}$$

where u and v are the axial (x–) and radial (r–) velocity components; p is the pressure; f_A is the mass fraction of argon in the argon–air mixture; and ρ, μ, h, k, c_p and U_r are the temperature- and composition-dependent plasma density, viscosity, specific enthalpy, thermal conductivity, specific heat at constant pressure and radiation power per unit volume of plasma, respectively. In Eq. (6), the last three terms represent the pressure work and viscous dissipation, which can be neglected only at low Mach numbers; all the terms containing $(h_A - h_B)$ represent the contribution of species diffusion to the energy transport [13, 35, 42], where h_A and h_B are the temperature-dependent specific enthalpies of gases A (argon) and B (air), respectively. J_x and J_r are the axial and radial components of the following argon (species A) diffusion mass flux vector [39, 40]

$$\mathbf{J}_A=-\left(n^2/\rho\right)\bar{m}_A\bar{m}_B\bar{D}^x_{AB}\nabla X_A-\bar{D}^T_{AB}\nabla\ln T \tag{8}$$

in which n is the total gas-particle number density, $\bar{m}_A$ and $\bar{m}_B$ are the averaged gas-particle masses for all the heavy particles (excluding electrons) coming from argon (i.e., species A) and those from air (i.e., species B), X_A is the molar fraction of argon in the argon–air mixture, whereas $\bar{D}^x_{AB}$ and $\bar{D}^T_{AB}$ are the combined ordinary diffusion coefficient associated with the argon mole-concentration gradient, ∇X_A, and the combined thermal diffusion coefficient associated with the temperature gradient, ∇T, respectively [39, 40]. The transport coefficient in the species conservation equation (7) can be expressed as $\Gamma_f=\left[\bar{m}_A\bar{m}_B/\left(\bar{M}\bar{M}_A\right)\right]\rho\bar{D}^x_{AB}$, in which $\bar{M}$ and $\bar{M}_A$ are the averaged gas-particle mass for all the gas particles (including electrons) of the gas mixture and that for all the gas particles coming from argon, respectively [39]. The source term S_f in Eq. (7) can be expressed as [35, 37, 41, 42]

$$\begin{aligned}S_f=&\frac{1}{r}\frac{\partial}{\partial r}\left(r\Gamma_f\frac{f_A}{\bar{M}}\frac{\partial\bar{M}}{\partial r}\right)-\frac{1}{r}\frac{\partial}{\partial r}\left(r\Gamma_f\frac{f_A}{\bar{M}_A}\frac{\partial\bar{M}_A}{\partial r}\right)+\frac{\partial}{\partial x}\left(\Gamma_f\frac{f_A}{\bar{M}}\frac{\partial\bar{M}}{\partial x}\right)\\&-\frac{\partial}{\partial x}\left(\Gamma_f\frac{f_A}{\bar{M}_A}\frac{\partial\bar{M}_A}{\partial x}\right)+\frac{1}{r}\frac{\partial}{\partial r}\left(r\bar{D}^T_{AB}\frac{\partial\ln T}{\partial r}\right)+\frac{\partial}{\partial x}\left(\bar{D}^T_{AB}\frac{\partial\ln T}{\partial x}\right)\end{aligned} \tag{9}$$

On the other hand, for the study of the characteristics of *turbulent* argon plasma jets issuing into the ambient air, Eqs. (3)–(9) are still be employed but all the physical quantities appearing in these equations are their time-averaged values. In addition, the molecular transport coefficients appearing in the conservation equations (4)–(7) are substituted by their counterparts containing both the turbulent and molecular contributions. Namely, μ in Eqs. (4) and (5) is substituted by $(\mu_t+\mu)$, k/c_p in Eq. (6) is substituted by $\left[\left(\mu_t/\mathrm{Pr}_h\right)+\left(k/c_p\right)\right]$, and Γ_f in Eq. (7) is substituted by $[\,(\mu_t/Sc_f)+\Gamma_f\,]$. In addition, an additional term representing the turbulent diffusion flux, i.e., $-\left(\mu_t/Sc_f\right)\nabla f_A$, is added into the right-hand side of Eq. (8) for the argon diffusion mass flux vector $\mathbf{J}_A$ [13]. Here μ_t is the turbulent viscosity and is calculated by $\mu_t=C_\mu\rho K^2/\varepsilon$ when the $K-\varepsilon$ two-equation turbulence model is employed. K and ε are the turbulent kinetic energy and its dissipation rate, and are solved by [12, 13, 35]:

$$\frac{\partial(\rho u K)}{\partial x}+\frac{1}{r}\frac{\partial(rv\rho K)}{\partial r}=\frac{\partial}{\partial x}\left[\left(\mu+\frac{\mu_t}{\mathrm{Pr}_K}\right)\frac{\partial K}{\partial x}\right]+\frac{1}{r}\frac{\partial}{\partial r}\left[r\left(\mu+\frac{\mu_t}{\mathrm{Pr}_K}\right)\frac{\partial K}{\partial r}\right]+G-\rho\varepsilon \tag{10}$$

$$\frac{\partial(\rho u\varepsilon)}{\partial x}+\frac{1}{r}\frac{\partial(rv\rho\varepsilon)}{\partial r}=\frac{\partial}{\partial x}\left[\left(\mu+\frac{\mu_t}{\mathrm{Pr}_\varepsilon}\right)\frac{\partial\varepsilon}{\partial x}\right]+\frac{1}{r}\frac{\partial}{\partial r}\left[r\left(\mu+\frac{\mu_t}{\mathrm{Pr}_\varepsilon}\right)\frac{\partial\varepsilon}{\partial r}\right]+\frac{\varepsilon}{K}(C_1G-C_2\rho\varepsilon) \tag{11}$$

$C_\mu, C_1, C_2, \mathrm{Pr}_h, Sc_f, \mathrm{Pr}_K$ and Pr_ε are constants in the turbulence model, and in this study they are taken to be their commonly adopted values, i.e., 0.09, 1.44, 1.92, 0.9, 1.0, 1.0 and 1.3, respectively. The turbulence generation term, G, in Eqs. (10) and (11) is calculated by

$$G=\mu_t\left[2\left(\frac{\partial u}{\partial x}\right)^2+2\left(\frac{\partial v}{\partial r}\right)^2+2\left(\frac{v}{r}\right)^2+\left(\frac{\partial u}{\partial r}+\frac{\partial v}{\partial x}\right)^2\right]. \tag{12}$$

The computational domain used in the modeling is denoted as A-B-C-D-E-A in Fig. 1. The radius of the jet inlet (A-B) is 4 mm. D-E is the flat substrate impinged by the plasma jet, and the radial size (DE or AC) of the computational domain is taken to be 50 mm, corresponding to typical conditions of plasma materials processing. The axial size (CD or AE) can vary in the range of 20–100 mm to investigate the effect of the distance between the flat substrate and the jet inlet (will be denoted by L and called the substrate standoff distance hereafter).

The boundary conditions used for the impinging jet modeling are as follows.

(i) At the jet inlet (A-B in Fig. 1): $v=0, f_A=1.0$, and the following profiles of axial velocity and temperature are used:

$$u=U_0[1-(r/R)^{1.4}],\quad T=(T_0-T_\mathrm{w})[1-(r/R)^{2.3}]+T_\mathrm{w} \tag{13}$$

in which R is the radius of the jet inlet (4 mm), T_w is the inner wall temperature of plasma torch and taken to be $T_\mathrm{w}=700$ K, whereas U_0 and T_0 are the maximum axial velocity and temperature at jet-inlet center (U_0 will be called the jet-inlet velocity and T_0 the jet-inlet temperature hereafter), respectively. For the turbulent cases, $K=0.00005\times u_\mathrm{in}^2$ and $\varepsilon=K^{3/2}/L_T$ are used at the jet inlet section A-B, where $L_T=0.075\delta_{0.1}/C_\mu^{3/4}$ and $\delta_{0.1}$ is the jet width defined by the radial distance at which the axial velocity reduces to $u=0.1\times U_0$ [12, 13, 35]. The jet-inlet axial-velocity and temperature profiles (13) were employed in a few previous studies [12, 13] and were shown to be able to predict plasma temperature, velocity and species concentration fields in reasonable agreement with corresponding experimental data for a typical turbulent argon plasma jet ($U_0=1092$ m/s and $T_0=12\,913$ K) issuing into the ambient air. For facilitating the comparison of laminar and turbulent plasma jet characteristics, the same jet-inlet velocity and temperature profiles are used in this study for both the laminar and turbulent plasma jets, as in [35].

(ii) At the rear surface B-C of the plasma torch wall, for the laminar case, $u=v=0$ and zero diffusion flux are employed, and the wall temperature is assumed to vary in the radial direction according to the relation $T=700-400\cdot[\ln(\mathrm{r}/\mathrm{R})/\ln(\mathrm{R_{out}}/\mathrm{R})]$, in which R and R_out are the inner-radius

and outer-radius of the plasma torch wall. For the turbulent jet case, wall function method is used to treat the B-C boundary conditions.

(iii) Along the outer free boundary C-D, the following conditions are employed:

$$\partial u/\partial r = 0, \quad \partial(\rho r v)/\partial r = 0,$$

and

$$\begin{aligned} &\text{if } v<0: T = 300\,\text{K}, \quad f_A = 0,\ K = 0,\ \varepsilon = 0 \\ &\text{if } v>0: \partial h/\partial r = 0, \quad \partial f_A/\partial r = 0,\ \partial K/\partial r = 0,\ \partial \varepsilon/\partial r = 0. \end{aligned} \tag{14}$$

(iv) At the plate surface D-E, for the laminar impinging jet case, $u = v = 0$ and zero diffusion flux are employed and the wall temperature is assumed to be 1,000 K. For the turbulent jet case, the wall function method is also used to treat the D-E boundary conditions. On the other hand, for the free jet cases (used for comparison with the impinging jets), one-way conditions are used at D-E, i.e., $\partial u/\partial x = 0$, $\partial v/\partial x = 0$, $\partial h/\partial x = 0$, $\partial f_A/\partial x = 0$ as well as (for the turbulent case) $\partial K/\partial x = 0$, $\partial \varepsilon/\partial x = 0$ will be used, as in [35].

(v) Along the jet axis A-E, the following axisymmetrical conditions are employed:

$$\partial \phi/\partial r = 0 \quad (\phi = u, h, f_A, K, \varepsilon), \quad v = 0. \tag{15}$$

The numerical solution method based on the SIMPLER algorithm [43] is used to solve the governing equations (3)–(7), (10) and (11) associated with correspondent boundary conditions. Namely, the control volume and finite difference methods are employed; the combined convection-diffusion terms are discretised using the power-law scheme formulated based on the exact solution of the one-dimensional convection -diffusion equation [43]; and the source terms are discretised using the central difference scheme. After the convergent results of the velocities, specific enthalpy, argon mass fraction and turbulent parameter (for turbulent case) fields in the plasma jets have been obtained, the temperature field can be easily calculated from the computed distributions of the specific enthalpy and argon mass fraction using the argon–air plasma property tables compiled for different temperatures (300–30,000 K with interval 100 K) and for different argon mass fractions at atmospheric pressure [40]. The grid points employed in the computation are $180(x-) \times 78$ (r-direction). Non-uniform mesh is adopted with finer mesh spacing near the plate surface, the jet inlet and the jet axis. A special numerical test shows that mesh-independent results have been obtained using the 180×78 mesh.

Results and Discussion

Typical computed results are presented in Figs. 2–9 concerning the characteristics of the subsonic argon plasma jets impinging normally upon a flat substrate located in atmospheric-pressure air surroundings for the laminar and turbulent flow regimes. In order to reveal more clearly the difference between the characteristics of laminar and turbulent impinging plasma jets, the same values of the U_0 and T_0 in the radial profiles (13) will be used at first for both the laminar and turbulent cases. After that the effects of different values of U_0 and T_0 are studied. It is noted that almost the

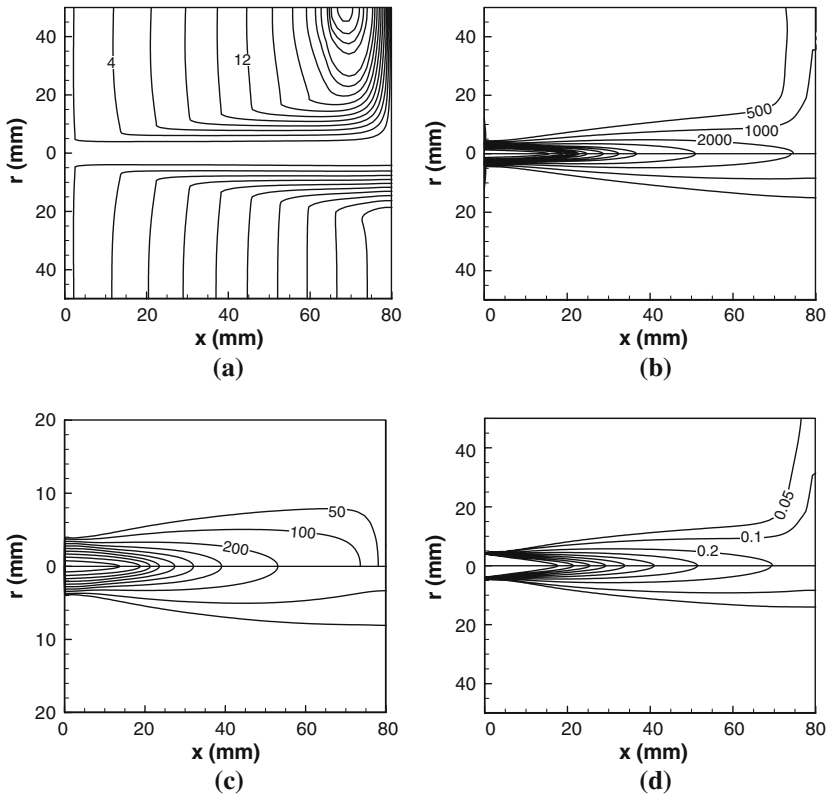

Fig. 2 Comparison of characteristics of turbulent impinging (upper semi-plane) and free (lower semi-plane) plasma jets. Jet-inlet temperature $T_0 = 14,000$ K, jet-inlet velocity $U_0 = 1,000$ m/s and substrate standoff distance $L =$ 80 mm. (**a**) Streamlines presented as 10^{-4} kg/s per radian, interval is 2×10^{-4} kg/s per radian; (**b**) isotherms in K, isotherm interval is 500 K for outmost two lines, 1,000 K for others; (**c**) isolines of axial velocity in m/s, interval is 50 m/s for outmost two lines, 100 m/s for others; and (**d**) isolines of argon mass fraction, interval is 0.05 for outmost two lines, 0.1 for others

same U_0 and T_0 values may be obtained in experiments for both the laminar and turbulent plasma jets by adopting special combinations of torch parameters [36].

For the case with the jet-inlet velocity $U_0 = 1,000$ m/s and jet-inlet temperature $T_0 = 14,000$ K, Figs. 2(a)–(d) compare the computed isolines of stream function, temperature, axial velocity and argon mass-fraction, respectively, in the turbulent plasma jet impinging upon the substrate with a standoff distance L = 80 mm (upper semi-plane) to those in corresponding turbulent free plasma jet without accounting for the existence of the substrate (lower semi-plane). Corresponding comparisons are shown in Figs. 3(a)–(d) for the laminar impinging plasma jet (upper semi-plane) and corresponding laminar free plasma jet (lower semi-plane). As is seen from the lower semi-planes of Figs. 2(a)–(d) and 3(a)–(d), due to the continuous entrainment of ambient air into the free plasma jets, the mass flow rate (directly proportional to the value of stream function shown in Fig. 2(a) or 3(a)) of the turbulent or laminar free plasma jet increases unceasingly, and the plasma temperature, axial velocity and argon mass fraction decrease in the direction of jet axis. Since the turbulent transport mechanism involved in the turbulent jet is much effective than the molecular diffusion

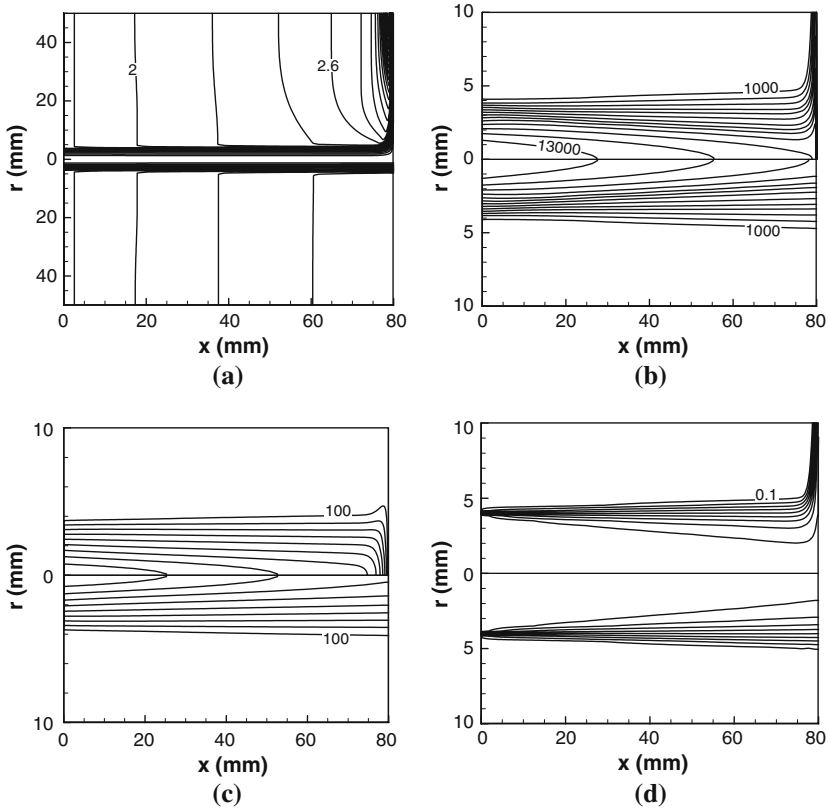

Fig. 3 Comparison of characteristics of laminar impinging (upper semi-plane) and free (lower semi-plane) plasma jets. $T_0 = 14,000$ K, $U_0 = 1,000$ m/s and $L = 80$ mm. (**a**) Streamlines presented as 10^{-4} kg/s per radian, interval is 2×10^{-5} kg/s per radian; (**b**) isotherms in K, interval is 1,000 K; (**c**) isolines of axial velocity in m/s, interval is 100 m/s; and (**d**) f_A isolines with interval 0.1

mechanism in the laminar jet, the mass flow rate of the ambient air entrained into the turbulent free plasma jet is much larger than that into the corresponding laminar free plasma jet and thus the effects of the air entrainment on the characteristics of the turbulent free plasma jet are much more significant than those of the laminar free plasma jet. As a result, similarly to that revealed in [35], the spreading angle of jet edge for the turbulent free plasma jet shown in Fig. 2(a) is appreciably larger than that for the laminar free plasma jet shown in Fig. 3(a); the axial decaying rates of plasma parameters (temperature, axial velocity and argon mass fraction) in the turbulent free plasma jet, as shown in the lower semi-planes of Figs. 2(b), (c) and (d), are much greater than those in the laminar free plasma jet shown in the lower semi-planes of Figs. 3(b), (c) and (d) (noting that different ordinate scales are used in those figures). Similar features are also applicable to the upstream regions of the turbulent and laminar impinging plasma jets, as seen from the upper semi-planes of Figs. 2(a)–(d) and 3(a)–(d). For example, in the upstream region with axial distances less than 50 mm, the flow, temperature and argon concentration fields in the impinging plasma jets are almost identical to those in the free plasma jets, i.e., the effects of substrate on the plasma jet characteristics can be completely neglected in

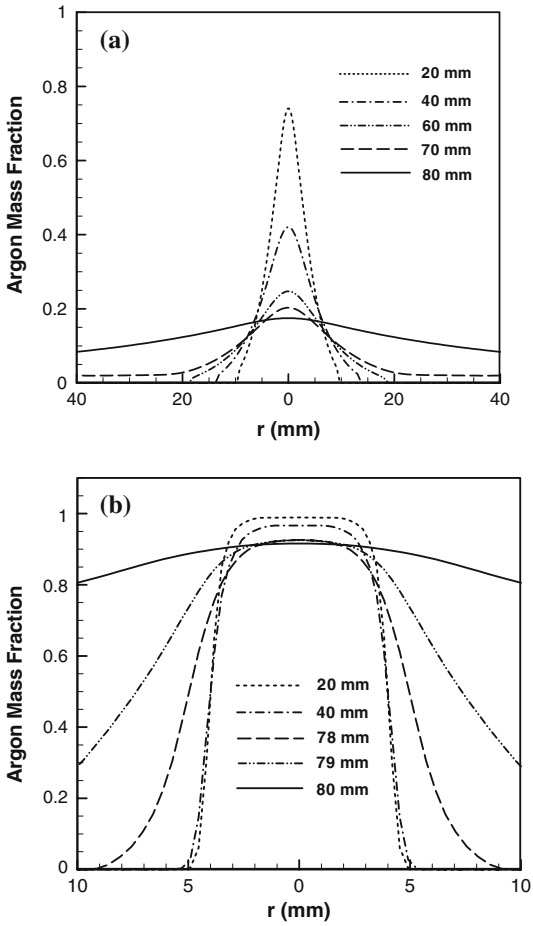

Fig. 4 Variations with the axial distance of the radial distributions of argon mass fraction in turbulent (**a**) and laminar (**b**) impinging plasma jets. $T_0 = 14,000$ K, $U_0 = 1,000$ m/s and L = 80 mm. The numerals in the figures denote the axial distances

the jet upstream regions. However, there is appreciable difference between the impinging and free plasma jets in their flow, temperature and concentration fields in the downstream or near-substrate region. Because the substrate forces the forward-flowing jet to change its flow direction, the flow fields in the vicinity of the substrate for the impinging plasma jet are quite different from those in corresponding free plasma jet (without accounting for the presence of substrate). Particularly, due to the formation and thickening of the radial wall jet along the substrate surface, the maximum mass flow rate of ambient air entrained into the impinging plasma jet is appreciably larger than that into the corresponding free plasma jet, and all the incoming plasma and entrained air turn to flow along the substrate surface and outflow radially from the computational domain. The temperature, axial velocity and argon mass fraction distributions in the near-substrate region for the impinging plasma jets are thus appreciably different from those in the corresponding free plasma jets, as shown in Figs. 2 and 3.

Figure 4 compares the radial distributions of argon mass fraction (f_A) at different axial locations in the turbulent and laminar impinging plasma jets for the case with L = 80 mm. As is seen, the radial profile of f_A widens and the central maximum

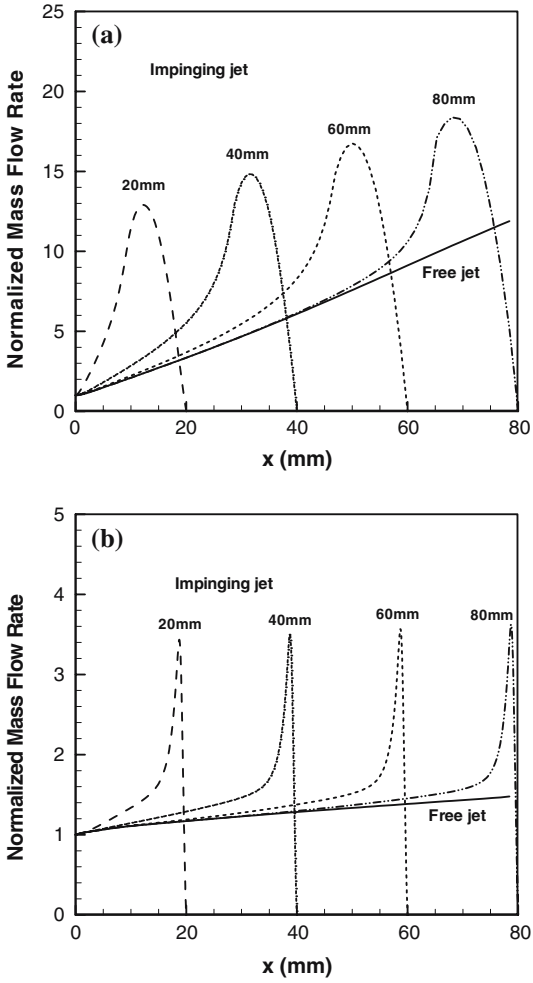

Fig. 5 Computed variations with the substrate standoff distance of normalized axial mass flux of the turbulent (**a**) and laminar (**b**) impinging plasma jets. Full line expresses the computed results of corresponding free plasma jets. $T_0 = 14,000$ K and $U_0 = 1,000$ m/s. Numerals in the figures are the substrate standoff distances

value of f_A decreases rapidly with increasing axial distance for the turbulent impinging plasma jet (Fig. 4(a)), while for the laminar impinging plasma jet rapid widening of the f_A profile only appears near the substrate surface (Fig. 4(b)). It is also seen that the f_A values in the vicinity of the substrate for the laminar impinging plasma jet are much larger than those for the turbulent impinging plasma jet. The calculated results in the upstream region of the turbulent impinging plasma jet (or for the free plasma jet) are approximately consistent with the experimental data and the modeling predictions presented in [11–13].

In order to better reveal the entrainment characteristics of the impinging and free plasma jets, in the following we use the x-dependent axial mass flux of the plasma jet calculated by

$$F = 2\pi \int_0^{R_{out}} \rho u r \, dr \ (R_{out} \text{ is the radius of computational domain}) \qquad (16)$$

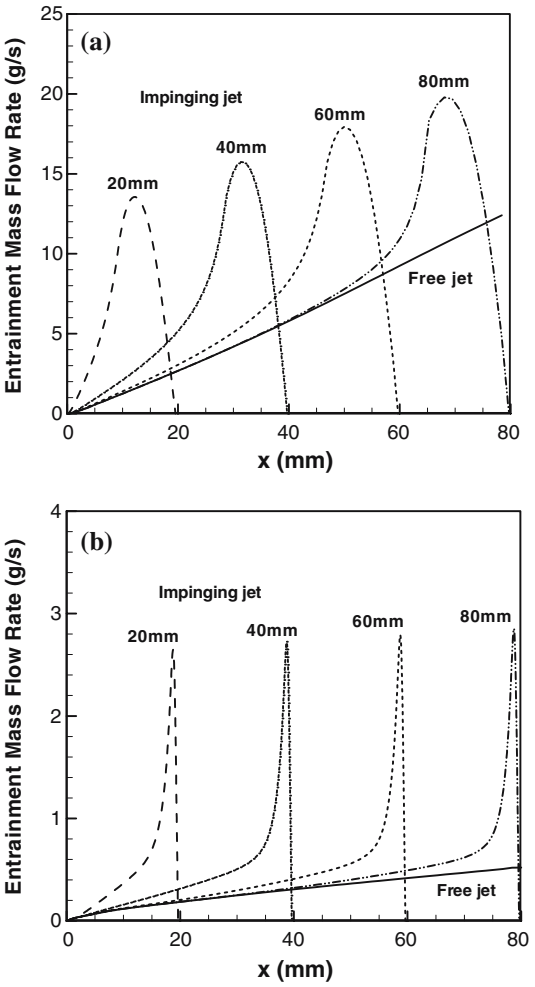

Fig. 6 Computed variations with the substrate standoff distance of the net mass flow rate entrained into the turbulent (**a**) and laminar (**b**) impinging plasma jets. Full line expresses the computed results of corresponding free plasma jets. $T_0 = 14,000$ K and $U_0 = 1,000$ m/s. Numerals in the figures are the substrate standoff distances

and the net mass flow rate of the ambient air entrained into the plasma jet calculated by

$$F_e = F - F_0 = 2\pi \int_0^{R_{out}} \rho u r \, dr - \left(2\pi \int_0^{R} \rho u r \, dr \right)_{inlet} \tag{17}$$

where $F_0 = (2\pi \int_0^R \rho u r \, dr)_{inlet}$ is the argon mass flow rate at the plasma jet inlet. For the case with the jet-inlet velocity $U_0 = 1,000$ m/s, jet-inlet temperature $T_0 = 14,000$ K and substrate standoff distances L = 20, 40, 60 and 80 mm, Fig. 5(a) compare the computed variations with the axial distance x from the jet inlet of the normalized axial mass fluxes

$$F/F_0 = 2\pi \int_0^{R_{out}} \rho u r \, dr / \left(2\pi \int_0^{R} \rho u r \, dr \right)_{inlet} \tag{18}$$

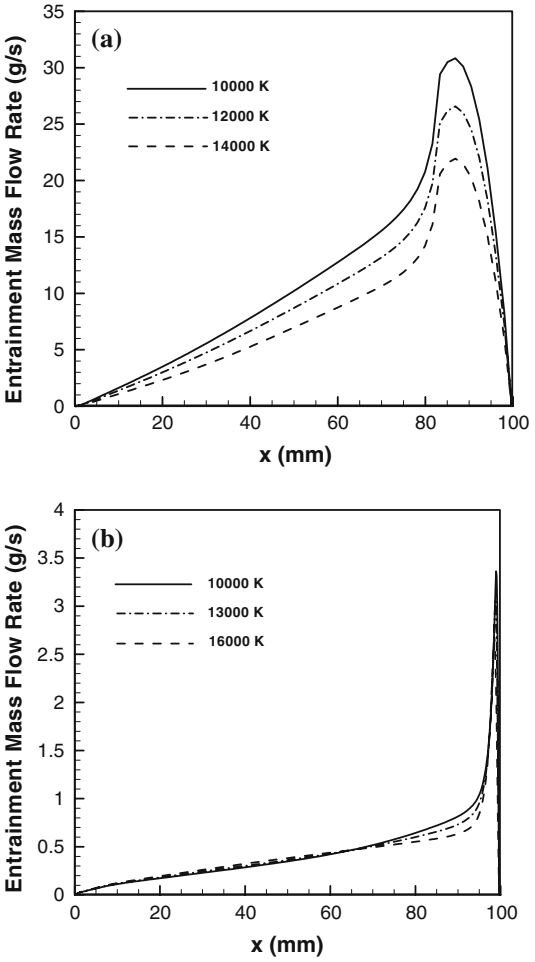

Fig. 7 Computed variations with the axial distance of the axial mass fluxes of the turbulent (**a**) and laminar (**b**) impinging plasma jets for different jet-inlet temperatures. $U_0 = 1,000$ m/s and $L = 100$ mm. $T_0 = 10,000$, 12,000 and 14,000 K for turbulent jets, whereas $T_0 = 10,000$, 13,000 and 16,000 K for laminar jets

for the turbulent impinging and free plasma jets. Corresponding comparisons are shown in Fig. 5(b) for the laminar impinging and free plasma jets. As is also seen from Figs. 5(a) and (b), for the case with the substrate standoff distance $L = 80$ mm, the variations with the axial distance of the normalized axial mass fluxes are almost the same in the upstream region (e.g., for the region with axial distance less than 50 mm) for both the impinging and free plasma jets. Significant effects of the substrate on the ambient-air entrainment only occur in the region near the substrate surface. Since the substrate forces the plasma jet to change its flow direction from axial to radial one, the axial mass flux in the impinging plasma jet assumes its maximum at a section ahead of the substrate and then decrease rapidly to zero at the substrate surface. The mass flow rate in the free plasma jet always increases monotonically in the axial direction for the turbulent free plasma jet, and Fig. 5(a) shows that at the axial section 80 mm from the jet inlet, the maximum axial mass flux is 12.5 times as large as the mass flow rate at the jet inlet ($F_0 = 1.087 \times 10^{-3}$ kg/s). On the other hand, the maximum axial mass flux for the turbulent impinging plasma

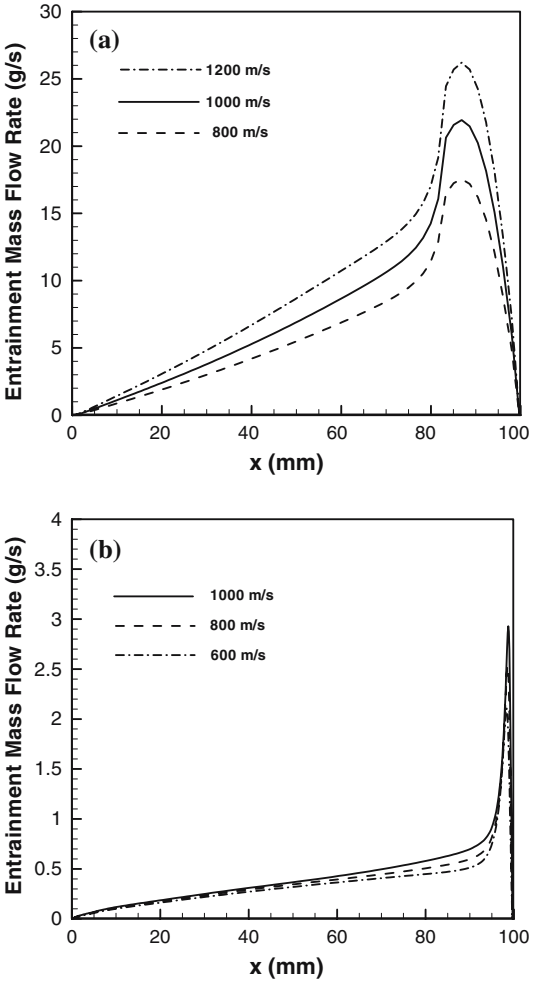

Fig. 8 Computed variations with the axial distance of the axial mass fluxes of the impinging plasma jets for different jet-inlet velocities. $T_0 = 14,000$ K and $L = 100$ mm. (**a**) Turbulent jets, $U_0 = 1,200$, 1,000 and 800 m/s; (**b**) laminar jets, $U_0 = 1,000$, 800 and 600 m/s

jet with substrate standoff distance L = 80 mm (the maximum flow-rate appears at the section ~ 12 mm ahead of the substrate surface) is 18.9 times as large as F_0, i.e., the air entrainment is enhanced due to the existence of the substrate and the enhancement factor of the axial mass flux caused by the additional entrainment of the wall jet for the turbulent impinging plasma jet is 1.51 (=18.9/12.5) for the case with L = 80 mm. The computed values of the enhancement factor are 1.85, 2.47 and 3.97 corresponding to the substrate standoff distances L = 60, 40 and 20 mm, respectively. The reason for the enhancement factor to decrease with increasing substrate standoff distance is that the mass flow rate entrained into the turbulent free plasma jet increases approximately linearly with increasing axial length, while the additional entrainment produced by the wall jet decreases with increasing substrate standoff distance. Correspondingly, Fig. 5(b) shows that the computed values of the enhancement factor of the axial mass flux caused by the additional entrainment of wall jet for the laminar impinging plasma jets are 2.94, 2.73, 2.58 and 2.45 for L = 20, 40, 60 and 80 mm, respectively. The enhancement factor for the laminar case also

decreases with increasing substrate standoff distance owing to the same reason as for the turbulent case. However, the decreasing rate of the enhancement factor with increasing substrate standoff distance for the laminar case is appreciably less than that for the turbulent case mainly due to that the increase rate of the mass flow rate with increasing axial distance for the laminar free plasma jet is much less than its turbulent counterpart while the decrease rate with increasing substrate standoff distance of the additional entrainment produced by the laminar wall jet is less than its turbulent counterpart.

Employment of the net entrained-air mass flow rate F_e calculated by Eq. (17) is more useful for clarifying the entrainment laws of the turbulent or laminar impinging and free plasma jets. For the case with the jet-inlet velocity $U_0 = 1,000$ m/s, jet-inlet temperature $T_0 = 14,000$ K and substrate standoff distances $L = 20$, 40, 60 and 80 mm, Fig. 6(a) compares the variations with axial distance of the computed values of the net entrained-air mass flow rates for the turbulent impinging and free plasma jets. Corresponding comparisons are shown in Fig. 6(b) for the laminar impinging and free plasma jets. As is seen from Fig. 6(a) and Table 1, at the sections with axial distances 20, 40, 60 and 80 mm from the jet inlet, the computed maximum values of the net entrained-air mass flow rate for turbulent impinging plasma jets, $(F_{em})_{t,imp}$, are 5.19, 2.75, 1.95 and 1.56 times, respectively, as large as their counterparts for the turbulent free plasma jets, $(F_{em})_{t,free}$. On the other hand, as is seen from Fig. 6(b) and Table 2, at the sections with axial distances 20, 40, 60 and 80 mm from the jet inlet, the computed maximum values of the net entrained-air mass flow rate for laminar impinging plasma jets, $(F_{em})_{l,imp}$, are 14.23, 8.84, 6.67 and 5.47 times, respectively, as large as their counterparts for the laminar free plasma jets, $(F_{em})_{l,free}$, respectively. It can also be seen that the maximum values of the net air mass flow-rate entrained into the turbulent impinging or free plasma jet is about one order of magnitude larger than their laminar counterparts. However, the *relative* contribution of the additional entrainment caused by the wall jet along the substrate surface for the laminar impinging plasma jet, i.e., $[(F_{em})_{l,imp} - (F_{em})_{l,free}]/(F_{em})_{l,free}$, is appreciably larger than its turbulent counterpart, i.e., $[(F_{em})_{t,imp} - (F_{em})_{t,free}]/(F_{em})_{t,free}$. For $L = 20$, 40, 60 and 80 mm, the values of former are 13.23, 7.84, 5.67 and 4.47, while the values of latter are 4.19, 1.75, 0.95 and 0.56, respectively. It means that the effect of the existence of the substrate on the air mass flow rate entrained into the laminar plasma jet is more significant than that into the turbulent plasma jet.

Table 1 Variations with the substrate standoff distance (L) of the computed maximum values of the mass flow rates entrained into turbulent impinging and free plasma jets[a]

Substrate standoff distance L	20 mm	40 mm	60 mm	80 mm
Impinging jet $(F_{em})_{t,\ imp}$ (10^{-3} kg/s)	13.69	15.63	17.72	19.49
Free jet $(F_{em})_{t,\ free}$ (10^{-3} kg/s)	2.64	5.68	9.10	12.48
Ratio $(F_{em})_{t,\ imp}$ / $(F_{em})_{t,\ free}$	5.19	2.75	1.95	1.56
Difference $(F_{em})_{t,\ imp}$–$(F_{em})_{t,\ free}$ (10^{-3} kg/s)	11.05	9.95	8.62	7.01
$(dF/dx)_{t,\ free}$ [10^{-3} kg/(s m)]	146	164	176	166

$T_0 = 14,000$ K, $U_0 = 1,000$ m/s and $F_0 = 1.087 \times 10^{-3}$ kg/s

[a] $(F_{em})_{t,imp}$ and $(F_{em})_{t,free}$ are the maximum values of the mass flow rates entrained into the turbulent impinging and free jets; $(dF/dx)_{t,free}$ is the local entrainment rate per unit length of turbulent free jet

Table 2 Variations with the substrate standoff distance (L) of the computed maximum values of the mass flow rates entrained into laminar impinging and free plasma jets[a]

Substrate standoff distance L	20 mm	40 mm	60 mm	80 mm
Impinging jet $(F_{em})_{l,\ imp}$ (10^{-3} kg/s)	2.647	2.724	2.790	2.852
Free jet $(F_{em})_{l,\ free}$ (10^{-3} kg/s)	0.186	0.308	0.418	0.521
Ratio $(F_{em})_{l,\ imp}/(F_{em})_{l,\ free}$	14.23	8.84	6.67	5.47
Difference $(F_{em})_{l,\ imp}$–$(F_{em})_{l,\ free}$ (10^{-3} kg/s)	2.461	2.416	2.372	2.331
$(dF/dx)_{l,\ free}$ [10^{-3} kg/(s m)]	6.40	5.74	5.33	5.21

$T_0 = 14,000$ K, $U_0 = 1,000$ m/s and $F_0 = 1.087 \times 10^{-3}$ kg/s

[a] $(F_{em})_{l,\ imp}$ and $(F_{em})_{l,\ free}$ are the maximum values of the mass flow rates entrained into the laminar impinging and free jets; $(dF/dx)_{l,\ free}$ is the local entrainment rate per unit length of the laminar free jet.

For the case with the jet-inlet velocity $U_0 = 1,000$ m/s and the substrate standoff distance $L = 100$ mm, Fig. 7 compares the axial variations of the net mass flow rate entrained into the turbulent (Fig. 7(a)) and laminar (Fig. 7(b)) impinging plasma jets for different jet-inlet temperatures (T_0 = 10,000, 12,000 and 14,000 K for the turbulent case, whereas T_0 = 10,000, 13,000 and 16,000 K for the laminar case). Figure 7(a) shows that for the turbulent impinging plasma jet, the maximum values of the net entrained-air mass flow rates $(F_{em})_{t,imp}$ decreases with increasing T_0 for the fixed U_0. The maximum values $(F_{em})_{t,imp}$ are $30.8 \times 10^{-3}, 26.6 \times 10^{-3}$ and 21.9×10^{-3} kg/s for the cases with $T_0 = 10,000$, 12,000 and 14,000 K. Since for $U_0 = 1,000$ m/s the jet-inlet mass flow rates corresponding to $T_0 = 10,000$, 12,000 and 14,000 K are $F_0 = 1.581 \times 10^{-3}, 1.314 \times 10^{-3}$ and 1.087×10^{-3} kg/s, respectively, the predicted results shown in Fig. 7(a) demonstrate that the maximum net air mass flow rate entrained into the turbulent impinging plasma jet, $(F_{em})_{t,imp}$, is approximately directly proportional to the argon mass flow-rate at the jet inlet (F_0). Such a prediction is consistent with that obtained in [35] for the turbulent free plasma jets, and even consistent with the prediction by Eq. (2) obtained for the turbulent free jets of cold gases [19–21]. On the other hand, Fig. 7(b) shows that corresponding to $T_0 = 10,000$, 13,000 and 16,000 K, the maximum values of the net air mass flow rate entrained into the laminar impinging plasma jet, $(F_{em})_{l,imp}$, are $3.36 \times 10^{-3}, 3.04 \times 10^{-3}$ and 2.68×10^{-3} kg/s, respectively, i.e., slightly decreases with increasing jet-inlet temperature. Such a predicted tendency is somewhat different from that obtained in [35] for the laminar free plasma jets, where the net entrained-air mass flow-rate was shown to increase slightly with increasing T_0.

For the case with the jet-inlet temperature $T_0 = 14,000$ K and the substrate standoff distance L = 100 mm, Fig. 8 compares the axial variations of the net mass flow rate entrained into the turbulent (Fig. 8(a)) and laminar (Fig. 8(b)) impinging plasma jets for different jet-inlet velocities (U_0 = 800, 1,000 and 1,200 m/s for the turbulent case, whereas $U_0 = 600$, 800 and 1,000 m/s for the laminar case). For the turbulent impinging plasma jets, corresponding to $U_0 = 800$, 1,000 and 1,200 m/s, the computed maximum values of the net mass flow rate entrained into the turbulent impinging plasma jets, $(F_{em})_{t,\ imp}$, are 17.6×10^{-3}, 21.9×10^{-3} and 26.2×10^{-3} kg/s, respectively, i.e., increase approximately in direct proportion to U_0 or to F_0 (the argon mass flow-rates at the inlet of the plasma jet). This prediction also agrees with the results obtained previously for the turbulent free plasma jets [35] and for the turbulent free jets of cold gases [19–21]. For the laminar impinging plasma jet,

Fig. 8(b) shows that the computed maximum value of the net entrained-mass flow rate, $(F_{em})_{l,imp}$, somewhat increases with increasing U_0. Corresponding to $U_0 = 600$, 800 and 1,000 m/s, the computed maximum net entrained-mass flow rates are 2.11×10^{-3}, 2.53×10^{-3} and 2.93×10^{-3} kg/s, respectively.

Tables 1 and 2 also give the calculated data of the local entrainment rate dF/dx for different axial distances and the difference between the maximum net air mass flow-rates entrained into the impinging and free jets, i.e., $[(F_{em})_{t,imp} - (F_{em})_{t,free}]$ for the turbulent flow regime and $[(F_{em})_{l,imp} - (F_{em})_{l,free}]$ for the laminar flow regime. It is seen from Tables 1 and 2 that although the additional contribution produced by the laminar wall jet along the substrate decreases with increasing axial distance, the decreasing rate is much less than its turbulent counterpart. The reason is that the axial decaying rates of plasma parameters (temperature, axial velocity, etc.) in the laminar plasma jet (where only molecular diffusion mechanism is involved) are much less than their counterparts in the turbulent plasma jet (where turbulent transport is dominant).

Although it is anticipated that Eqs. (1) and (2) obtained for laminar and turbulent free jets of cold gases are not completely applicable to the highly non-isothermal thermal plasma jets, it is found that they are still useful for understanding the entrainment of ambient air into the thermal plasma jets. For example, Eq. (2) shows that the mass flow rate entrained into a turbulent free gas jet is directly proportional to the jet-inlet mass flow-rate, which is also approximately applicable to the turbulent free or impinging plasma jet, as discussed above. Hence, it is worthy to examine whether Eqs. (1) and (2) can be used to estimate roughly the mass flow rate of the ambient air entrained into the thermal plasma jet. For $T_0 = 14,000$ K and $U_0 = 1,000$ m/s, the local entrainment rates per unit length of the laminar free plasma jet, $(dF/dx)_{l,free}$, are 6.40×10^{-3}, 5.74×10^{-3}, 5.33×10^{-3} and 5.21×10^{-3} kg/(s m), corresponding to the axial distances of 20, 40, 60 and 80 mm. If we assume Eq. (1) is applicable to estimate the local entrainment rate of the laminar free plasma jet, corresponding to those $(dF/dx)_{l,\ free}$ values, the values of the effective viscosity estimated by using Eq. (1) will be 2.55×10^{-4}, 2.28×10^{-4}, 2.12×10^{-4} and 2.07×10^{-4} Pa s. These estimated values of the effective viscosity seem to be reasonable if one notices that corresponding to temperatures 9,000, 10,000 and 11,000 K, the values of viscosity are 2.33×10^{-4}, 2.43×10^{-4} and 2.35×10^{-4} Pa s for air and 2.50×10^{-4}, 2.63×10^{-4} and 2.59×10^{-4} Pa s for argon [40] and that argon–air mixture is involved in the mixing layer of the laminar plasma jet. On the other hand, noting that here $D_0 = 8 \times 10^{-3}$ m, $F_0 = 1.087 \times 10^{-3}$ kg/s, $\rho_0 = 2.47 \times 10^{-2}$ kg/m^3 (argon at 14,000 K) and $\rho_a = 1.18$ kg/m^3 (air at room temperature), if we use Eq. (2) to estimate the entrainment coefficient $C = (D_0/F_0)(\rho_0/\rho_a)^{1/2}(dF/dx)_{t,free}$ from the computed $(dF/dx)_{t,free}$ values listed in Table 1, the values of the entrainment coefficient C would be 0.156, 0.175, 0.187 and 0.177, corresponding to L = 20, 40, 60 and 80 mm, respectively. Those values of the entrainment coefficient C are all within the range of 0.1–0.32 obtained for turbulent free jets of cold gases [19–21], and thus seem also to be reasonable.

Equations (1) and (2) cannot be used to estimate the entrainment rates of the laminar and turbulent impinging plasma jets, since the additional entrainment rates caused by the wall jet in the impinging plasma jets depend on the radial size of the employed computational domain. Considering that the radius of the intensely heated region in plasma materials processing is usually of tens millimeters, the radial size of the computational domain is chosen to be 50 mm in this study. If a computational

domain with larger radial size is used, the computed maximum mass flow rate of the ambient air entrained into the impinging plasma jet would increase, since more air would be entrained into the wider wall jet region. However, such an additional air entrainment of the wall jet with larger radial distance does not affect appreciably the flow, temperature and argon concentration fields in the central region of the impinging plasma jets, and thus less influences the plasma materials processing.

The present study concerning the air entrainment laws, besides its academic sense, is expected to be helpful to improve plasma materials processing. For example, this study reveals that the existence of substrate significantly enhances the mass flow rate of ambient air entrained into the impinging plasma jet, which means that employing a gas or solid shroud in torch design [8, 10, 16] is only useful for preventing the entrainment of ambient air into the main jet region but cannot appreciably reduce the air entrainment into the wall jet formed along the substrate surface.

The engulfment-type entrainment mechanism has been revealed in [3, 5], implying that the turbulent free plasma jet is of heterogeneous features (i.e., consisting of two different kinds of fluid parcels with different temperatures and transported from the jet inlet and the ambient fluid, respectively). Huang et al. [7] used a two-fluid model to study the characteristics of a turbulent free argon plasma jet issuing into argon surroundings. It was found that the predicted results of the two-fluid model are consistent with corresponding experimental data, including the radial and axial profiles of the time-averaged plasma temperature and axial-velocity in the jet. The radial distributions of plasma axial-velocity and temperature at successive cross-sections with different axial distances from the jet inlet were shown to be able to correlated, respectively, by the following non-dimensional Gauss-type expressions

$$u/u_{\mathrm{c}} = \exp\left[-(\ln 2)\eta_u^2\right] \tag{19}$$

$$(T - T_{\mathrm{a}})/(T_{\mathrm{c}} - T_{\mathrm{a}}) = \exp\left[-(\ln 2)\eta_T^2\right], \tag{20}$$

where u_{c} and T_{c} are the axial velocity and temperature at the jet axis on the cross-section; T_{a} is the ambient temperature; non-dimensional radial coordinate $\eta_u = r/\delta_u$, in which δ_u is the radial distance corresponding to $u/u_{\mathrm{c}} = 1/2$, while $\eta_T = r/\delta_T$, in which δ_T is the radial distance corresponding to $(T - T_{\mathrm{a}})/(T_{\mathrm{c}} - T_{\mathrm{a}}) = 1/2$. In our study it is found that Eqs. (19) and (20) are also applicable to describing the modeling results of the turbulent free plasma jet, as seen from the left semi-planes of Figs. 9(a) and (b), although the turbulence model employed in this study is quite different from that used in Ref. [7] and the turbulent free argon plasma jet studied here is issuing into air instead of argon surroundings in [7]. This fact means that the present modeling results also agree with the experimental data of W. Chen cited in [7]. Additionally, the left semi-plane of Fig. 9(c) shows that the radial distributions of argon mass fractions in the turbulent free jet can also be correlated by using the following Gauss-type expression:

$$f_A/f_{A,\mathrm{c}} = \exp\left[-(\ln 2)\eta_f^2\right] \tag{21}$$

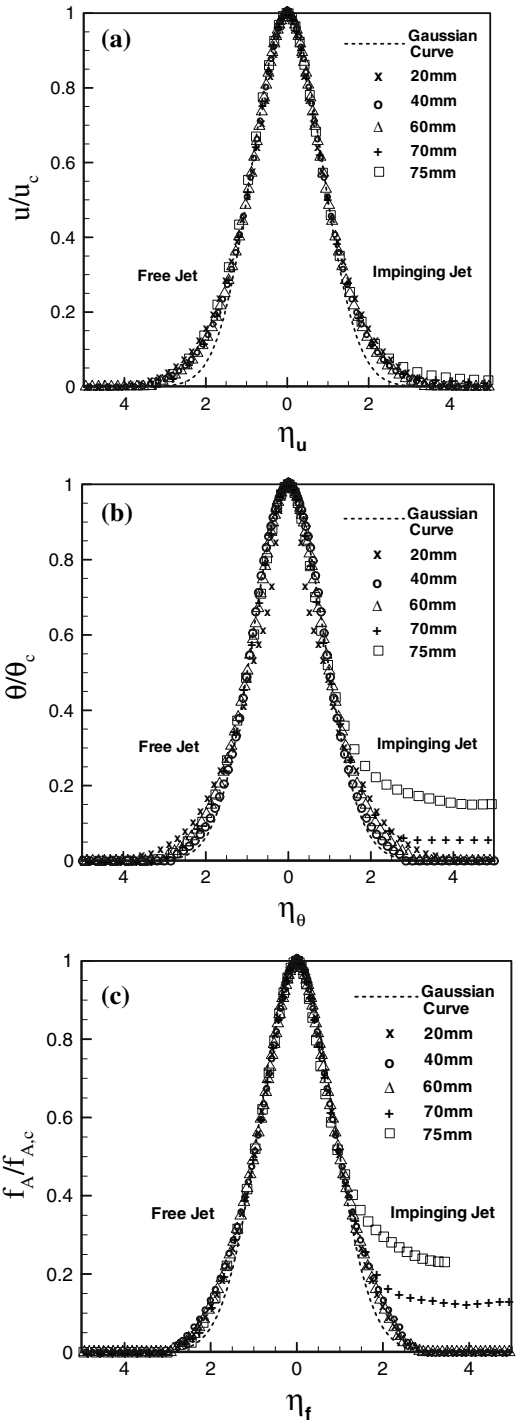

Fig. 9 Comparisons of the non-dimensional radial distributions of the axial velocity (**a**), temperature (**b**) and argon mass fraction (**c**) in the turbulent free (left semi-planes) and impinging (right semi-planes) plasma jets. $T_0 = 14,000$ K, $U_0 = 1,000$ m/s and $L = 80$ mm

where $f_{A,c}$ is the argon mass fraction at the jet axis in the cross-section and $\eta_f = r/\delta_f$, in which δ_f is the radial distance corresponding to $f_A/f_{A,c} = 1/2$. Moreover, Fig. 9 compares the radial profiles of computed axial-velocities, temperatures and argon mass fractions for the turbulent free (left semi-plane) and impinging (right semi-plane) plasma jets. It is seen that except for the near-substrate region, the difference between the turbulent free and impinging jet characteristics is small, i.e., the Gauss-type correlations (19)–(21) are also applicable to describing the radial profiles of plasma parameters in the upstream region of the turbulent impinging plasma jet.

It is expected that the arc-root movement at the anode surface of a DC arc plasma torch [14] will result in time-dependent entrainment characteristics. Ref. [44] performed a time-dependent three-dimensional (3-D) modeling study concerning the arc rotation within the DC arc plasma torch under the action of externally applied magnetic field, while Refs. [45, 46] carried out time-dependent 3-D modeling studies for the plasma torches working at the re-strike mode [45] and the takeover mode [46], respectively. Fluctuations of plasma parameters even exist in the DC arc plasma torch used for generating the long laminar plasma jets [47]. Since this study is only concerned with the quasi-steady entrainment features of plasma jets, how the time-dependent temperature and velocity profiles at the torch exit affects the entrainment law of ambient air into the plasma jets cannot been revealed and should be taken as the topic of further studies.

Conclusions

Modeling results are presented concerning the special features of the entrainment of ambient air into subsonic laminar and turbulent impinging or free argon plasma jets. It is found that the existence of the substrate enhances significantly the mass flow rate of the ambient air entrained into the plasma jet due to the additional contribution to the gas entrainment of the wall jet formed along the substrate surface. The plasma temperature, velocity and species concentration distributions in the near-substrate region are also influenced by the substrate. The maximum mass flow-rate of ambient air entrained into a turbulent impinging plasma jet is approximately directly proportional to the mass flow rate at the jet inlet, while its laminar counterpart slightly decreases with increasing jet-inlet temperature but increases with increasing jet-inlet velocity. The fraction of the additional entrainment caused by the wall jet in the total entrained-air flow rate for the laminar impinging plasma jet is appreciably larger than its turbulent counterpart. The entrainment rate expressions (1) and (2) established for laminar and turbulent free jets of cold gases can be used to estimate roughly the entrainment rates of laminar and turbulent free plasma jets, provided that a suitable value of the effective gas viscosity is chosen in Eq. (1) for the laminar plasma jet and a reasonable value of the entrainment coefficient is used in Eq. (2) for the turbulent plasma jet.

Acknowledgments This work was supported by the National Natural Science Foundation of China (Nos. 50336010, 10575127, 10405015). The authors would like to thank Dr. A. B. Murphy who provides us the property tables for the argon–air plasmas.

References

1. El-Kaddah N, McKelliget J, Szekely J (1984) Metallurg Trans B 15B: 59
2. Chyou Y P, Pfender E (1989) Plasma Chem Plasma Process 9:291
3. Pfender E, Fincke J, Spores E (1991) Plasma Chem Plasma Process 11:529
4. Chang CH, Ramshaw JD (1993) Plasma Chem Plasma Process 13:189
5. Pfender E (1994) Thin Solid Films 238:228
6. Fincke JR, Chang CH, Swank WD, Haggard DC (1994) Int J Heat Mass Transfer 37:1673
7. Huang PC, Heberlein J, Pfender E (1995) Plasma Chem Plasma Process 15:25
8. Kang KD, Hong SH (1999) J Appl Phy 85:6373
9. Li HP, Chen Xi (2002) Plasma Chem Plasma Process 22:27
10. Gawne DT, Zhang T, Liu B (2002) Surf Coat Technol 153:138
11. Fincke JR, Crawford DM, Snyder SC, Swank WD, Haggard DC, Williamson RL (2003) Int J Heat and Mass Transfer 46:4201
12. Williamson RL, Fincke JR, Crawford DM, Snyder SC, Swank WD, Haggard DC (2003) Int J Heat Mass Transfer 46:4215
13. Cheng K, Chen Xi (2004) Int J Heat Mass Transfer 47:5139
14. Fauchais P (2004) J Phys D Appl Phys 37:R86
15. Xiong HB, Zheng LL, Sampath S, Williamson RL, Fincke JR (2004) Int J Heat Mass Transfer 47:5189
16. Cheng K, Chen Xi, Wang HX, Pan WX (2006) Thin Solid Films 506–507:724
17. Schlichting H (1979) Boundary layer theory, 7th edn. McGraw-Hill, New York, pp 230–234
18. Loitsyanski LG (1963) Laminar boundary layer, Physico-Mathematic Literature, Moscow, pp 167–172 (in Russian)
19. Ricou FP, Spalding DB (1961) J Fluid Mech 11:21
20. Hill BJ (1972) J Fluid Mech 51:773
21. Han DH, Mungal MG (2001) Combust Flame 124:370
22. Garimella SV, Rice RA (1995) J Heat Transfer 117:871
23. Fitzgerald JA, Garimella SV (1998) Int J Heat Mass Transfer 41:1025
24. Glauert MB (1956) J Fluid Mech 1:21
25. Bakke P (1957) J Fluid Mech 2:467
26. Deshpande MD, Vaishnav RN (1982) J Fluid Mech 114:213
27. Aihara T, Kim JK, Maruyama S (1990) Wärme- und Stoffübertragung 25:145
28. Park TK (2003) Int J. Heat Mass Transfer 46:251
29. Osaki K, Fukumasa O (2000) Vacuum 59:47
30. Pan WX, Zhang WHua, Zhang WHong, Wu CK (2001) Plasma Chem Plasma Process 21:23
31. Pan WX, Zhang WH, Ma W, Wu CK (2002) Plasma Chem Plasma Process 22:271
32. Pan WX, Li G, Meng X, Ma W, Wu C K (2005) Pure Appl Chem 77:373
33. Pan WX, Meng X, Li G, Fei QX, Wu CK (2005) Surf Coat Technol 197:345
34. Ma W, Pan WX, Wu CK (2005) Surf Coat Technol 191:166
35. Cheng K, Chen Xi, Pan WX (2006) Plasma Chem Plasma Process 26:211
36. Pan WX, Meng X, Chen Xi, Wu CK (2006) Plasma Chem Plasma Process 26:335
37. Cheng K, Chen Xi (2004) J Phys D Appl Phys 37:2385
38. Xu DY, Chen Xi, Pan WX (2005) Int J Heat Mass Transfer 48:3253
39. Murphy AB (1993) Phys Rev E 48:3594
40. Murphy AB (1995) Plasma Chem Plasma Process 15:279
41. Xu DY, Chen Xi, Cheng K (2003) J Phys D Appl Phys 36:1583
42. Xu DY, Chen Xi (2005) Int Commun Heat Mass Transfer 32:939
43. Patankar SV (1980) Numerical heat transfer and fluid flow. McGraw-Hill, New York
44. Park JM, Kim KS, Hwang TH, Hong SH (2004) IEEE Trans Plasma Sci. 32:479
45. Moreau E, Chazelas C, Mariaux G, Vardelle A, Modeling the restrike mode operation of a DC plasma spray torch, Paper in Proc 2006 Int. Thermal spray Conf., May 15–18, Seattle
46. Trelles JP, Pfender E, Heberlein J (2006) Multiscale finite element modeling of arc dynamics in a DC plasma torch, Plasma Chem Plasma Process. 26:557
47. Chen Xi, Pan WX, Meng X, Cheng K, Xu DY, Wu CK (2006) Pure Appl Chem 78: 1253